Journal of Solid State Chemistry 181 (2008) 1552–1559

Contents lists available at ScienceDirect

Journal of Solid State Chemistry

journal homepage: www.elsevier.com/locate/jssc

Recent developments in synthetic approaches to transition metal phosphide nanoparticles for magnetic and catalytic applications

Stephanie L. Brock *, Keerthi Senevirathne

Department of Chemistry, Wayne State University, Detroit, MI 48202, USA

ARTICLE INFO

Article history:
Received 27 January 2008
Received in revised form
5 March 2008
Accepted 10 March 2008
Available online 26 March 2008

Keywords:
Metal phosphides
Nanoparticle synthesis
Size- and shape-dependent magnetic properties
Hydrodesulfurization catalysis

ABSTRACT

Recent advances in synthetic methods have led to the preparation of a wide array of transition metal phosphide nanoparticles, and characterization of these materials has provided insight into nanoscale magnetic and catalytic properties. This review highlights advances in the field that have been made since the time of the last review [S.L. Brock, S.C. Perera, K.L. Stamm, Chem. Eur. J. 10(2004)3364–3371]. Synthetic methods include solvothermal, solution-phase arrested precipitation, metal nanoparticle conversion, and phosphate reduction. Magnetic properties of FeP, Fe_2P and MnP nanoparticles and nanorods (among others), and recent data on thiophene hydrodesulfurization catalyzed by discrete, unsupported Ni_2P particles, is presented. Finally, the future prospects for the field are discussed.

1. Introduction

Transition metal phosphides are a class of compounds that exhibit a range of properties of fundamental and commercial interest, depending on their phase. For example, Fe_3P is a ferromagnet with a high transition temperature ($T_C = 692$ K) [1], whereas FeP_2 is a small bandgap semiconductor [2]; orthorhombic MoRuP is a superconductor ($T_C = 15$ K) [3], the filled phosphide skutterudites (e.g., $CeFe_4P_{12}$) exhibit promising thermoelectric properties [4], and Ni_2P is among the most active catalysts for hydrodesulfurization (HDS) [5]. These properties are often augmented on the nanoscale, providing an impetus for developing synthetic methods that enable preparation of discrete nanoparticles with control of size, shape and phase. In 2004, the last time transition metal phosphide nanoparticles were reviewed [6], very few methods had been explored for synthesis of transition metal phosphide nanoparticles other than solvothermal syntheses and reduction of phosphate salts on high surface area supports, with the latter method focused on generating catalytic materials for HDS. What little research was being conducted on discrete phosphide nanoparticles prepared by solution-phase methods was focused largely on main group metals, such as InP and GaP [7]. The 4 years that have elapsed since the last review have seen considerable advances in synthetic methods for transition metal phosphide nanomaterials, and these have enabled the magnetic and catalytic properties to be evaluated in some detail. The present review will describe recent advances in the synthesis of transition metal phosphide nanomaterials, with emphasis on discrete (unaggregated and unsupported) phases. The current understanding of the size- and phase-dependent magnetic properties will be discussed, as will the potential for discrete phosphide nanoparticles to address key factors in HDS catalyst activity. Many of the phases that have been studied most extensively, and therefore form the bulk of this review, fall into two main structure types, the MnP and Fe_2P structure types. These are illustrated in Fig. 1.

2. Synthetic approaches

Synthetic strategies for making metal phosphide nanostructures are taking a new face as various methodologies are discovered and used. In addition to describing advances in solvothermal methods, new approaches for preparing discrete nanoparticles, including arrested precipitation reactions and transformation of discrete metal particles to phosphides, will be presented. Finally, methods such as sonochemistry, confinement in carbon nanotubes (CNT), and reduction in templates, will be discussed.

2.1. Solvothermal methods

Solvothermal routes are less popular than they were several years ago for making transition metal phosphide nanoparticles

* Corresponding author. Fax: +1 313 577 8822.
E-mail address: sbrock@chem.wayne.edu (S.L. Brock).

0022-4596/$ - see front matter © 2008 Elsevier Inc. All rights reserved.
doi:10.1016/j.jssc.2008.03.012

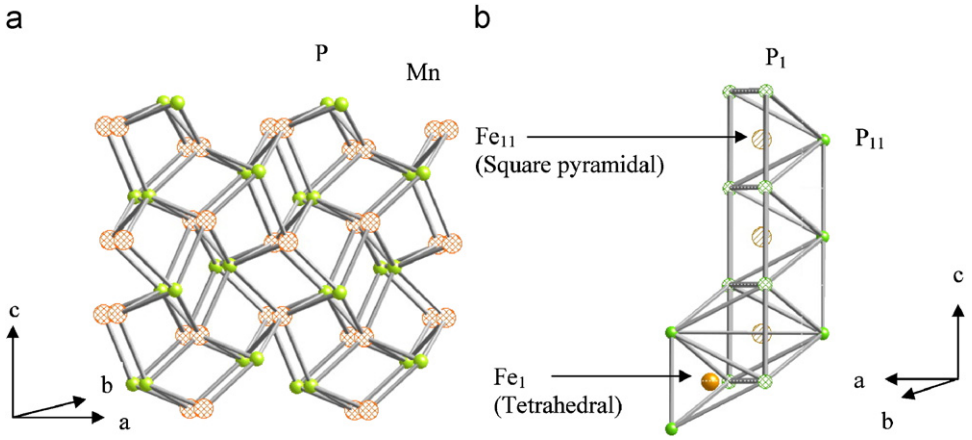

Fig. 1. Illustration of the structure types for (a) MnP (FeP, CoP) and (b) Fe_2P (Ni_2P) and relevant phosphides that crystallize in these structure types. The MnP structure type can be viewed as a distorted (orthorhombic) variant of the hexagonal NiAs structure type [39]. The Fe_2P structure type consists of a hexagonal arrangement of canals of alternating filled and empty square pyramids and tetrahedra pairs. The Co_2P structure (not shown) has the same local structure as Fe_2P, but the canals form a zig-zag stacking arrangement, resulting in an orthorhombic lattice [58].

[6], and few new phases have been reported. However, this approach has been exploited to make new particle and aggregate morphologies, including dendrites and hollow spheres and tubes. Reaction of nickel sulfate with yellow phosphorus in glycol/water at 180 °C yields dendritic nanostructures of Ni_2P [8], whereas a similar reaction with $CoCl_2$ in aqueous ammonia at 220 °C yields Co_2P nanorods [9]. In both cases, the anisotropic structures appear to grow from large, micron-sized spheres, consistent with a similar growth mechanism for the two cases that involves transformation of discrete nanoparticles to large aggregates (spheres), growth of rods from the spheres, transformation of rods into dendrites, and growth of dendrites at the expense of spheres [8]. Discrete nanoparticle aggregation has also led to micron-sized hollow spheres and tubes of Cu_3P [10] and Co_2P [11] and likely plays a role in $Ni_{12}P_5$ hollow sphere formation using CTAB as a structure directing agent [12]. The mechanism of formation of hollow structures in systems that do not have structure directing surfactants remains unknown, but has been postulated to arise from bubble formation during the course of the reaction [11]. Solvent phase separation may provide an alternate explanation, but no convincing evidence is put forth for any mechanism.

2.2. *Synthesis of nanorods and spherical particles from injection/slow heating of molecular precursors*

Despite their promise, solvothermal reactions suffer from a number of drawbacks when it comes to nanoparticle synthesis. Most notably, the products are lacking in monodispersity and are aggregated, rather than disperse, making it difficult to study their size-dependent physical properties. For this reason, there has been considerable focus on adapting methods used to make monodisperse quantum dots, such as CdSe, to transition metal phosphides. Originally applied to FeP and MnP spherical nanoparticles [6,13,14], a host of new phases have been prepared by this approach in the last 4 years. The general method involves reaction of metal and phosphorus precursors at high temperature and in a coordinating solvent, such as trioctylphosphine oxide (TOPO). Thus, discrete 4.7 ± 0.7 nm particles of FeP were prepared by reaction of $Fe(acac)_3$ with $P(SiMe_3)_3$ in TOPO at 260 °C [13], whereas 5.1 ± 0.5 and 6.7 ± 0.3 nm MnP particles were prepared by reaction of $Mn_2(CO)_{10}$ with $P(SiMe_3)_3$ at 220 and 250 °C, respectively [14]. Subsequently, it has been shown that many metal precursors are sufficiently reactive to confiscate phosphorus from considerably less reactive sources than $P(SiMe_3)_3$, such as trioctylphosphine (TOP), and even tetradecylphosphonic acid (TDPA). The use of strongly coordinating solvents, such as TOP, also facilitates formation of anisotropic structures by allowing high reagent concentrations that favor anisotropic growth in crystals where the crystallographic planes have different chemical potentials. As noted in Table 1, and described below, this approach has been successful in preparing nanorods and wires of a range of metal phosphides.

Discrete nanorods of iron phosphides were independently reported by three groups in 2004. The groups of Hyeon and Liu exploited the reaction of $Fe(CO)_5$ with TOP to prepare Fe_2P [15] and FeP nanorods [16], respectively; whereas the group of Chi used pre-reacted $(\eta^4\text{-}C_6H_8)Fe(CO)_3$ with TOP, presumably proceeding via iron nanoparticle intermediates, to prepare FeP nanorods [17]. The specific factors that govern which phase will form remain unclear, although both the solvent system and the temperature of the reaction are presumed to play a role. Thus, Hyeon obtained Fe_2P when using oleylamine (OA) and octylether (OE) as solvents at temperatures of 300 °C [15], whereas TOPO at much higher temperatures (360 °C) leads to FeP [18]. In contrast to reactions with $P(SiMe_3)_3$, reactions with TOP require higher temperatures (>300 °C) due to the fact that more energy is required to break the P–C bond, a necessary step in the liberation of active phosphorus from TOP, than the P–Si bond of $P(SiMe_3)_3$.

As indicated above, one critical factor related to nanorod/wire formation is maintaining a high concentration of reagents in solution. This can be achieved by starting with a high concentration (facilitated by strong binding ligands), sequential injection of additional precursor aliquots over the course of the reaction to maintain the concentration, or continuous injection of reagents. The Hyeon method applies continuous injection, and the length of the rods is related to the rate of the injection. Hyeon and co-workers have also employed this method for the formation of FeP, MnP, Co_2P and Ni_2P nanorods [18]. Intriguingly, the correlation between the length of the rods/wires and the injection rate depends on the identity of the metal. Thus, faster rates of injection lead to longer rods in the case of MnP, but shorter rods for Fe_2P [18]. This may be related to the relative reactivity of the metal complexes.

Nanorods prepared by high temperature injection appear to form as single crystals, although the growth direction has not been established in every case. Hyeon and co-workers report that MnP and Co_2P nanorods grow perpendicular to the (002) planes (i.e., along *c*), FeP nanowires grow perpendicular to the (013)

Table 1
Transition metal nanorods and nanowires prepared from molecular precursors

Phase	Synthetic conditions[a]	Dimensions (nm)	Ref.
MnP	$Mn_2(CO)_{10}$/TOP to TOPO at 330 °C, cont. injection, 18 h	6×22, 8×16, 11×15	[18]
	$Mn_2(CO)_{10}$/ODE to TOP/TOPO at 350 °C, 1–5 h	5×20	[19]
Fe_2P	$Fe(CO)_5$/TOP in OE/OA at 300 °C, stepwise or cont. injection, $\leqslant 3$ h	3×12, $5–6 \times 43–290$	[15]
	$H_2Fe_3(CO)_9P^tBu$ in TOA/OAc, slow heating to 315–330 °C, 20 min	6×70 and ca. $50–100 \times 500$+nm split bundles	[22]
FeP	$Fe(CO)_5$/TOP/TOPO, >300 °C stepwise injection of Fe precursor in TOP, 0.5–8 h	$5 \times 20–2000$	[16]
	$Fe(CO)_5$/TOP/TOPO at 330–360 °C, cont. injection, 0.5 h	7×600, 12×500	[18]
	$(\eta^4\text{-}C_6H_8)Fe(CO)_3$/TOPO at 340 °C, stepwise injection of $(\eta^4\text{-}C_6H_8)Fe(CO)_3$ and TOP	$5 \times$ hundreds	[17]
Co_2P	$Co(acac)_2$/TOP in OE/HDA at 300 °C, cont. injection, 1 h	2.5×20	[18]
	$CpCo(CO)_2$ or Cp_2Co/TOP in OE/OA at 300 °C, cont. injection	6×22, 5×20	[18]
CoP	$Co(acac)_2$/TDPA/TOPO/HDA at 340 °C, 3 h	10×100, 7×400	[57]
Ni_2P	$Ni(acac)_2$/TOP to TOPO at 330 °C, cont. injection, 1 h	4×9	[18]

[a] TOP = trioctylphosphine; TOPO = trioctylphosphine oxide; ODE = octadecene; OA = oleylamine; OAc = oleic acid; OE = octylether; TOA = trioctylamine; HDA = hexadecylamine, acac = acetylacetonate; Cp = cyclopenadienyl.

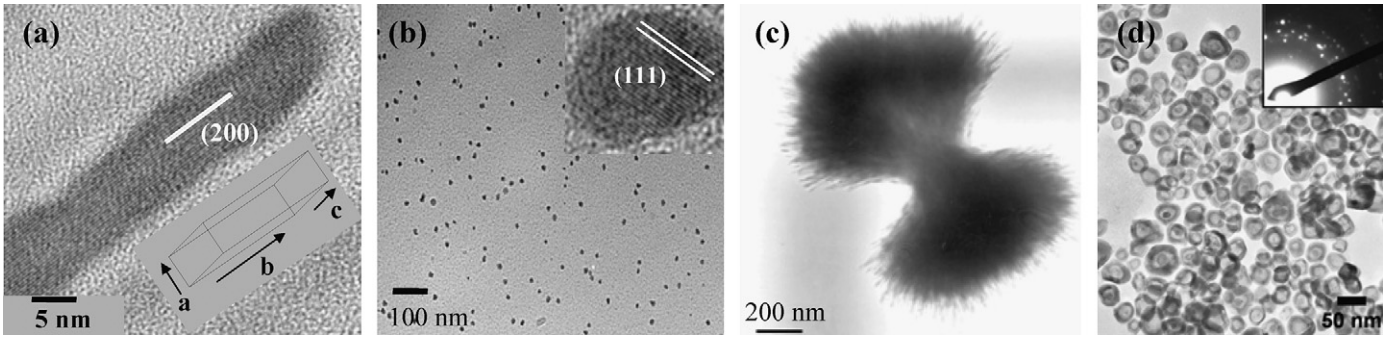

Fig. 2. TEM images of (a) a nanorod of MnP, (b) discrete Ni_2P nanoparticles, (c) fibrous dumbbells of Fe_2P and (d) hollow Ni_2P spheres and corresponding selected area electron diffraction pattern. Reproduced with permission from Ref. [19] (panel a, copyright 2006 American Chemical Society), Ref. [20] (panel b, copyright 2007 Wiley-VCH Verlag GmbH & Co. KGaA), Ref. [22] (panel c, copyright 2007 American Chemical Society), and Ref. [23] (panel d, copyright 2007 American Chemical Society).

planes, and Ni_2P nanorods grow perpendicular to the (300) planes (along *a*). While continuous injection adds a measure of control to the reactions, it does not appear to be critical for rod formation. Brock and co-workers have prepared MnP nanorods ($20.3 \pm 3.6 \times 5.20 \pm 0.89\ nm^2$) with narrow polydispersities by a single rapid injection of $Mn_2(CO)_{10}$ in octadecene into TOP/TOPO [19]. Careful analysis of HRTEM images has established that growth in this system occurs along the *b*-axis of the orthorhombic MnP-type phase (Fig. 2a), in contrast to observations of the rods prepared by Hyeon and co-workers. Injection of aliquots leads to longer rods and wires, but the samples are polydisperse. Post-annealing at lower temperatures than the nucleation temperature leads to formation of cubes, apparently by assembly of rods, although this could also be an example of crystal splitting.

Spherical nanoparticles result with the reactive phosphine, $P(SiMe_3)_3$ (MnP [14], FeP [13]), or upon rapid injection of precursors when the less reactive TOP is used (Ni_2P (Fig. 2b) [20], Co_2P [18]). This can be explained by rapid nucleation at the initially high concentration of reactants (or due to the very high reactivity of the source), followed by a precipitous decrease in concentration that will favor 3-D, in lieu of 1-D, growth [21].

In addition to using individual metal and phosphorus precursors, Whitmire and co-workers have shown that single source precursors can be employed [22]. With the goal of controlling the final phosphide stoichiometry by using a precursor with the desired metal to phosphorus ratio, $H_2Fe_3(CO)_9P^tBu$ (**1**) was investigated as a precursor to Fe_3P. However, the final products obtained from decomposition of **1** in trioctylamine (TOA) and oleic acid (OAc) are nanorods and bundles of Fe_2P. An IR study of the products of thermolysis as a function of temperature reveals that **1** transforms to $Fe_4(CO)_{12}(P^tBu)_2$ at 140 °C, presumably liberating $Fe(CO)_5$, and this may explain the formation of Fe_2P in lieu of Fe_3P. However, the stability of the clusters in the presence of solvent at elevated temperatures remains unknown, and it is possible that they break into Fe- and P-containing fragments that then combine at the nucleation temperature. Upon decreasing the TOA:OAc ratio, larger crystallites form and undergo splitting, giving the appearance of bundles of rods. T and cross-shaped bundles form due to twin formation. Intriguingly, when alkanes are added to the mixture, crystal splitting phenomena lead to fibrous dumbbell shapes, or sheathes (Fig. 2c).

2.3. Transformation of metal nanoparticles to metal phosphide nanoparticles and hollow spheres

An alternate approach to metal phosphide nanoparticle synthesis is to start with metal particles and transform them into phosphides by reaction with phosphines. The synthesis of FeP nanowires by Chi and co-workers, mentioned above, is postulated to proceed by this route [17]. The authors first react $(\eta^4\text{-}C_6H_8)Fe(CO)_3$ in TOPO at 340 °C, presumably forming Fe nanoparticles, and then inject aliquots of $(\eta^4\text{-}C_6H_8)Fe(CO)_3$ in TOP into this mixture. The product forms as nanorods or nanowires, depending

on the quantity of iron precursor in the injection aliquot. However, the presence of discrete Fe nanoparticles as an intermediate phase, while postulated, was not verified.

In 2007, the groups of Schaak and Chiang reported that Ni nanoparticles could be transformed into Ni_2P nanoparticles by treatment with TOP [23,24]. Furthermore, depending on the size of the precursor nanoparticles and/or the concentration of TOP, hollow Ni_2P structures can be produced due to the Kirkendall effect (Fig. 2d) [23,24]. This mechanism presumes a solid-state reaction in which the rate of diffusion of metal atoms from the interior occurs more rapidly than the influx of phosphorus atoms generated at the exterior by breakdown of TOP. Thus, Ni atoms are rapidly depleted from the core, yielding a hollow structure. The size of the hollows is therefore dependent on the diffusion distance as well as the difference of diffusion rates, such that very small particles produce no hollows at all. Thus, 5.2 nm Ni nanoparticles yield 5.6 nm dense Ni_2P particles, whereas 10–20 nm Ni particles transform into hollow Ni_2P particles, and particles that are larger still give particles encapsulated within the hollow structures [23]. An additional factor in the solid-state transformation is the corrosive nature of TOP towards metal atoms. Thus, Chiang and co-workers noted that the use of pure TOP led to solid particles even when relatively large (12 nm) precursor particles were employed, and that reproducible hollow structure formation requires dilution of TOP with another solvent, such as 1-octadecene, along with the use of a non-reactive metal binding agent, such as OA [24]. This suggests that dense structures may form by dissolution of the metal particles and reprecipitation as phosphide when the TOP concentration is large, thereby obviating the solid-state Kirkendall mechanism and hollow particle formation.

When active, the solid-state mechanism permits the morphology of the starting particle to be retained. Thus, cubes, triangles and multipods of Rh_2P can be generated by treatment of Rh nanoparticles of the corresponding morphology with TOP in the presence of suitable co-solvents to bridge the miscibility gap between the PVP stabilized Rh nanoparticles and the TOP reactant (PVP and TOP are not miscible) [25]. One must be careful to avoid too active a co-solvent in order to avoid TOP etching effects. Likewise, high temperatures result in aggregated particles with loss of shape, although the high temperature facilitates complete conversion of the metal to the phosphide. The loss of particle shape is likely due to metal dissolution, at least from reactive corners and edges, and reprecipitation. It is challenging to balance these two effects to form shape-controlled particles of Rh_2P, while ensuring that the conversion of Rh is complete, thus the Rh_2P product is often contaminated by Rh metal.

This method of metal conversion is extremely versatile, and has been applied to the preparation of nanoparticles of FeP, CoP, Co_2P, Cu_3P, AgP_2, PtP_2, PdP_2, Pd_5P_2 and Au_2P_3 [23,24,26]. It has also been applied to thin films, supported nanoparticles, and even patterned substrates, foils and wires of metals to yield the corresponding phosphide, extending the method to formation of Ni_5P_4, Zn_3P_2, CuP_2, GaP, and InP [26].

2.4. Other methods

Formation of iron, nickel–iron and iron–cobalt phosphide nanoparticles has been achieved in carbon nanotubes (CNT) by the use of thin metal films deposited on anodic alumina membranes followed by treatment with carbon precursors to yield metal phosphide nanoparticles encapsulated in CNT [27]. The phosphorus source appears to be impurities in the anodized alumina. The resultant materials look like matchsticks: CNT with metal phosphide particles encapsulated periodically along the axis of the CNT. The nanoparticles appear to adopt the Fe_2P structure type, based on selected area electron diffraction patterns, and have dimensions of $10–60 \times 25–100\,nm^2$. The elongated dimension of the particle corresponds to the axial direction of the CNT.

FeP coated on Fe_3O_4 nanoparticles, as well as hollow FeP shells, has been prepared by the sonochemical reaction of $Fe(CO)_5$ with TOP in TOPO in air [28]. Centrifugation of the mixture after 4 h of reaction yields the core-shell particles as the precipitate and the FeP nanoshells as the dispersed phase. The core-shell particles have 5–10 nm cores and 2–3 nm shells whereas the hollow particles have outer diameters of 5–10 nm and empty cores of 3–8 nm. Presumably, the iron oxide cores arise from air oxidation in the course of the reaction.

Reduction methods have been extensively performed for metal phosphide nanoparticle preparation, particularly for formation of supported phosphides for catalysts. The general reduction method involves treatment of metal phosphates with H_2 at high temperature, and this approach has been shown to be amenable to a range of transition metals with suitable reduction potentials [29,30]. Recently, solution-phase deposition of iron phosphate inside anodized alumina templates with pore diameters of 200 nm has yielded Fe_3P nanocomposites upon hydrogen reduction at 650–800 °C [31]. Epoxy attachment of the membrane to a support followed by NaOH dissolution of the alumina template yields nanowire composites of epoxy with Fe_3P particles embedded within. The ability to form nanocrystalline Fe_3P, the only iron phosphide that is ferromagnetic with a T_C above room temperature, has yet to be achieved using precipitation routes.

3. Magnetic properties

Interest in ferromagnetic nanoparticles in general stems from their potential applications in magnetic storage, magnetic refrigeration, MRI enhancement, and site-directed drug-delivery, among others. The unique properties of ferromagnetic nanoparticles arise from their size-dependent coercivity in the critical regime 1–100 nm [32,33]. A decrease in particle size to that of a single domain results in an increase in coercivity, the field required to demagnetize the ordered magnet, due to a change in mechanism for reorientation of spins in the magnetic field from one of domain wall migration to coherent spin rotation. However, as the size is decreased below single domain, the magnetic particles are subject to thermal fluctuation, or superparamagnetism, and exhibit zero coercivity, although they still have the characteristic saturation behavior of a ferromagnet. The transition from a superparamagnetic state to a coercive state occurs at the blocking temperature T_b. T_b is size dependent, but also depends strongly on the intrinsic magnetocrystalline anisotropy of the sample (preferred direction of spin orientation), as well as shape anisotropy. There has been considerable interest in designing rod and wire structures of ferromagnetic materials because the shape anisotropy contributes to augmented coercivity and increased blocking temperature, permitting stable magnetic bits to be created with small cross-sectional areas [34]. The blocking temperature is experimentally determined from evaluation of the temperature-dependent susceptibility acquired at low applied field in a zero-field cooled (ZFC) sample, and is manifest as a maximum in the ZFC plot. The intersection of the ZFC and field-cooled (FC) plot is the irreversibility temperature (T_{irr}). In narrow polydispersity samples, $T_{irr} = T_b$.

The focus of magnetic studies in nanoscale transition metal phosphides has been on phases of iron and manganese. Among the iron phosphides, FeP (Fig. 1a) exhibits a unique magnetic structure consisting of a helical arrangement of spins with net

antiferromagnetic ordering and a Néel temperature (T_N) of 120 K [35,36]. Fe_2P (Fig. 1b) is a ferromagnet with a Curie temperature (T_C) of 209 K, but exhibits a large degree of short-range order above this temperature, manifest in a Weiss constant of ca. 400 K [1]. The magnetic properties of Fe_2P are strongly dependent on the presence of defects (non-stoichiometry or substitutional) and T_C values ranging up to 306 K have been reported [37]. Fe_3P is also ferromagnetic, with a T_C of 692 K [38]. Like its structural analog, FeP, MnP exhibits helimagnetic ordering at low temperature with a T_N of 47 K; however, MnP is ferromagnetic above T_N with a T_C of 292 K [39].

FeP: The prior work of Brock and co-workers on ca. 5 nm FeP nanoparticles revealed that the helimagnetic transition is completely suppressed in the nanoparticles, which is ascribed to an inability to sustain order in nanocrystals with dimensions that approach that of the magnetic unit cell (the ordering axis for the helimagnet is ca. 2.9 nm in length) [13]. Instead, Curie–Weiss behavior is observed down to ca. 75 K, the Weiss constant is −28 K, consistent with local antiferromagnetic interactions, and the moment is 2.98 μ_B. No hysteresis was observed in magnetization vs. field plots. Consistent with these results, Liu and co-workers also noted an absence of ordering for FeP nanorods that had a similar diameter to those reported by Brock and co-workers (5 nm) and aspect ratios varying up to 200 [16]. They observe Curie–Weiss behavior down to 10 K with a Weiss constant of −10 K, and a smaller moment (0.7 μ_B). They did note the presence of a ferromagnetic impurity with an apparent T_C of 270 K, and attribute this to clusters of Fe_2P or Fe, consisting of a mass percent of <0.1%.

In contrast to expectation, other groups report ferromagnetic behavior for FeP nanorods. Hyeon and co-workers observed a blocking temperature of 350 K for $11 \times 450\ nm^2$ rods of FeP and large coercivities of 8200 Oe [18]. Examination of graphs provided by Chi and co-workers for 5 nm diameter FeP rods suggest a T_B of ca. 145 K and the large difference between T_B and T_{irr} suggests the samples are not very uniform [17]. Two nanometer shells of FeP formed around 5 to 10 nm diameter hollow spheres also appear to be ferromagnetic, with a coercivity of 760 Oe at 5 K and about 7 Oe at room temperature. This can be modified by inclusion of a soft ferromagnetic material in the core. Thus, with 5–10 nm Fe_3O_4 cores wrapped by 2–3 nm FeP shells, the coercivity is smaller (ca. 500 Oe) than for the shells alone. There are a number of possible explanations for the unexpected ferromagnetic properties observed in FeP nanomaterials. The presence of uncompensated spins on the surface of antiferromagnetic materials has been shown to give rise to an apparent ferromagnetic response [40]. It is also possible that the response is due to the presence of a small quantity of ferromagnetic impurity phase, as Liu and co-workers have noted [16].

Fe_2P: Fe_2P nanowires and bundles also exhibit ferromagnetic properties, although sometimes with an anomalously high T_b (i.e., greater than $T_C = 217$ K). Hyeon and co-workers observed size-dependent blocking temperatures ranging from 75 to 250 K for a series of rods with cross-sections of 5–6 nm and lengths from 43 to 290 nm [15]. Chemical analyses indicate an iron-rich phase is also present. Fe_3P ($T_C = 692$ K) or Fe ($T_C = 1043$ K) impurities at levels <2% of the total volume could account for some of the observed response. Nanowires and bundles of Fe_2P prepared by Whitmire and co-workers also exhibit a variation in T_b from 124 to 205 K, depending on whether discrete nanorods ($T_b = 124$ K) or bundles of rods ($T_b = 180$–205 K) were probed, and T_b and T_{irr} separate as the bundles get larger, presumably due to a distribution in the size of the magnetic contributors [22]. These trends are consistent with strong dipolar coupling within the bundles. Intriguingly, *M* vs. *H* data show that coercivity persists up to 250 K, which may be due to a ferromagnetic impurity such as Fe or Fe_3P, but may also be a consequence of the strong short-range order intrinsic to Fe_2P [1].

MnP: Both Hyeon and co-workers and Brock and co-workers have investigated the magnetic properties of MnP nanoparticles. Like FeP, there is no evidence of helimagnetic ordering in the magnetic response for any of the MnP nanoparticle samples. Instead, MnP is ferromagnetic and coercive, even below T_N (the helimagnetic–ferromagnetic phase transition). Spherical MnP nanoparticles exhibit a large coercivity at 5 K (ca. 6000 Oe) and a size-dependent blocking temperature ($T_b = 60.8$ K for 5.1 ± 0.5 nm spheres, $T_b = 74.3$ K for 6.7 ± 0.3 nm spheres) [14]. Hyeon and co-workers observed a similar response for two MnP rod samples (8×16 and $11 \times 25\ nm^2$), a T_b approaching T_C (260 K) and a coercivity of 5000 Oe at 15 K [18]. These nanocrystals are reported to form with the axial growth direction coincident with the *c*-axis. Surprisingly, data reported by Gregg et al. on MnP nanorods of dimension $5.2 \pm 0.89 \times 20.3 \pm 3.6\ nm^2$, but grown along *b*, exhibit a similar coercivity (4200 Oe at 10 K) and blocking temperature ($T_b = 250.4$ K) to that reported by Hyeon and co-workers (Fig. 3) [19]. Given the fact that MnP has a magnetocrystalline easy axis along *c*, one would anticipate that growth in this direction would lead to a significantly augmented coercivity and T_b relative to rods grown in other directions. However, nearly identical behavior is observed when comparing data from Hyeon and co-workers (grown along *c*) with Gregg et al. (grown along *b*) and while the T_b is much increased relative to spherical particles, the coercivity is, if anything, decreased. Indeed, an evaluation of the anisotropy constants for MnP nanoparticle samples suggests very little difference between the spherical particles and rods [19]. That is, the augmented T_b can be attributed entirely to volume differences between the spheres and rods, not to a contribution from shape anisotropy. This may explain the lack of a concomitant increase in coercivity. The absence of shape anisotropy in MnP is unexpected, and suggests that the intrinsic magnetocrystalline anisotropy is the dominant effect in this system.

The disparity between the properties of bulk MnP and its nanoparticle forms, in particular the lack of a metamagnetic response at low temperature due to the helimagnetic structure of the bulk phase, has contributed to confusion regarding the origin of room temperature ferromagnetism in Mn-doped chalcopyrites, such as $CdGaP_2$:Mn. A careful analysis of Mn-doped chalcopyrite samples of $CdSnP_2$:Mn exhibiting room temperature coupling suggests that the properties arise from MnP nanoparticle formation in the course of the reaction, not from carrier-mediated coupling, as is desired in a diluted magnetic semiconductor [41]. Furthermore, an identical response can be obtained from the products of low-temperature reactions of CdP_2, or even red phosphorus, with Mn, suggesting that the phase responsible for the ferromagnetic response is not an intrinsically doped phase, but rather a phase separated one (MnP).

Co_2P, Ni_2P: Hyeon and co-workers also investigated the magnetic properties of Ni_2P and Co_2P nanorods, observing a Curie–Weiss response at high temperatures (>200 K) and very large Weiss constants (−370 K) indicative of antiferromagnetic short-range order [18]. Bulk phases of Ni_2P and Co_2P are Pauli paramagnets and exhibit a susceptibility that is independent of temperature. It is possible that the observed response reflects a combination of Pauli paramagnetism with uncompensated spins on the particle surface to yield these unusual properties. Xie and co-workers also report a Curie–Weiss response for their Co_2P nanorods, although few details are provided [9].

4. Catalytic properties

The development of new HDS and hydrodenitrogenation (HDN) catalysts has become particularly important in the face of legislation reducing allowable sulfur and nitrogen levels in fuels,

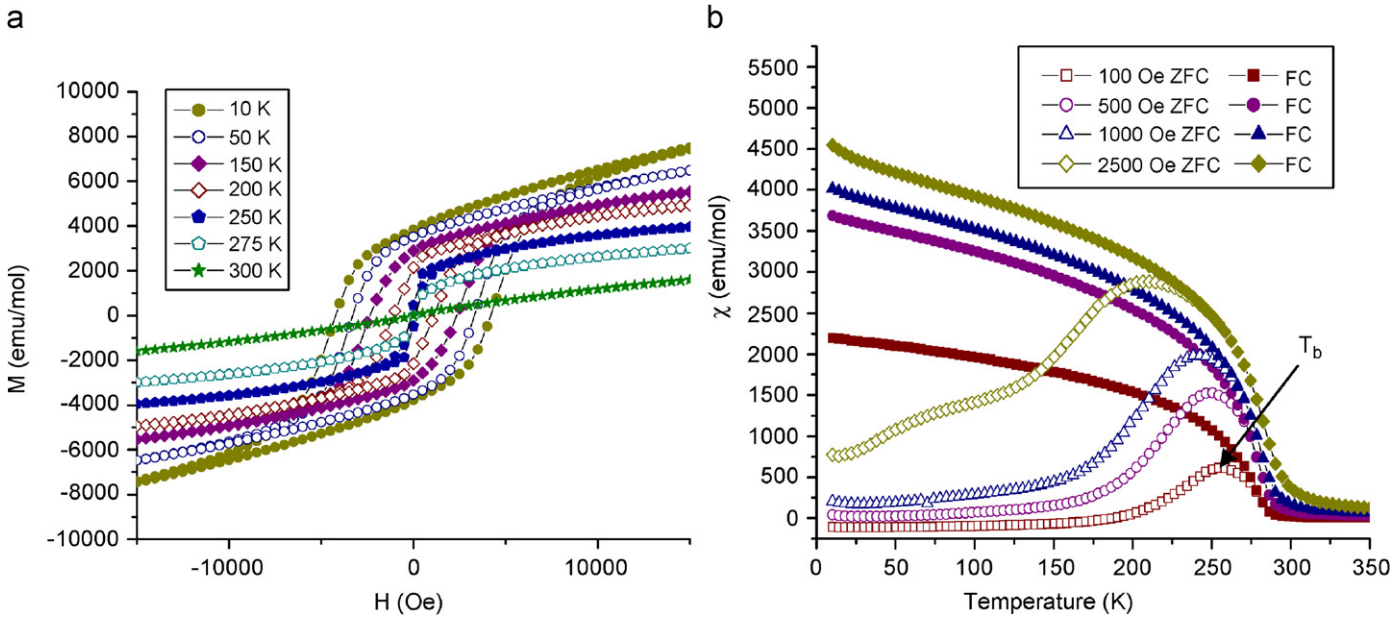

Fig. 3. Magnetic data for a MnP $20.3 \times 5.2\,nm^2$ rod sample: (a) a magnetization vs. field graph for temperatures varying from 10 to 300 K. (b) Zero-field cooled (ZFC) and field cooled (FC) susceptibility data acquired at applied fields varying from 100 to 2500 Oe. Reproduced with permission from Ref. [19] (Copyright 2006 American Chemical Society).

and the transition from sources of crude from Saudi Arabia to less pure sources derived from Canadian oil sands [42]. It is unclear that further engineering of the commercial catalyst of choice, alumina-supported sulfided molybdenum, will be able to address the increased catalyst demand. Hence, efforts are underway to develop new catalysts for hydrotreating, and transition metal phosphides have shown significant promise in this regard [5,20,43–56]. Among transition metal phosphides, Ni_2P materials have exhibited the highest activity and resistance to poisoning [5]. With few exceptions, these reports have focused on the catalytic activity of supported catalysts that are typically prepared by impregnation of metal phosphates in solution on silica or alumina support, followed by reduction with H_2 (the temperature-programmed reduction (TPR) method) or in situ during catalysis. Recently, other methods have been explored, including treatment of silica or alumina-supported Ni or NiO particles, or Ni–B amorphous alloys, with PH_3/H_2 at 150–350 °C [43,47]; or treatment of Ni nanoparticles supported on graphite with TOP solution at 300 °C [26].

As indicated previously, hydrogen reduction of transition metal phosphates typically requires high temperatures, upwards of 580 °C. Korányi as well as Berhault and co-workers have instead explored nickel thiophosphate ($NiPS_3$) to generate unsupported nickel phosphides at lower temperatures, exploiting the more facile cleavage of the P–S bond relative to the P–O bond. Intriguingly, there are distinct differences between the behavior of crystalline $NiPS_3$ and an amorphous precursor prepared at room temperature from reaction of nickel nitrate with Li_2PS_3 in water [50]. Crystalline $NiPS_3$ transforms initially to Ni_5P_4 beginning at 400 °C, Ni_2P starts to appear at 500 °C and the product is single phase Ni_2P by 600 °C. In contrast, amorphous $NiPS_3$ transforms at low temperature to Ni_2P (300 °C), and produces single phase Ni_2P by 400 °C. Continued heating leads to formation of Ni_5P_4 (450 °C) and single-phase, highly crystalline Ni_2P is recovered at 600 °C. Judging from X-ray broadening, the amorphous precursor also permits recovery of a less crystalline Ni_2P product, which may be advantageous for catalytic applications. The surface area of the aggregated nanocrystalline products ranged from 21 to $30\,m^2/g$, and these materials exhibit four times the intrinsic activity to HDS of thiophene (Th) as MoS_2 [50]. Unsupported Ni_2P catalysts with a considerably higher surface area have been prepared using a new method in which ethylene glycol and a polymer surfactant (Triton X-114) were included in the reaction mixture with nickel nitrate and ammonium monohydrogen phosphate [44]. Reduction of the solid product at 400–500 °C in flowing H_2 yielded Ni_2P nanostructures with surface areas as high as $130\,m^2/g$.

While TPR and related approaches have been successful in preparing catalysts with higher activities than the current generation of sulfided molybdenum catalysts [5], these methods pose several disadvantages when it comes to preparing test systems for evaluating the microstructural characteristics that underpin the activity. Specifically, the size of the particles cannot be controlled with any accuracy, making estimations of turnover frequencies difficult, nor is it straightforward to assess the relative reactivities of crystal faces. Furthermore, the TPR method itself is poorly suited for preparing alumina-supported phosphide catalysts, because of the high reactivity of alumina towards phosphate, generating aluminum phosphate.

The recent development of solution-phase methods that enable formation of monodisperse samples of transition metal phosphide nanoparticles of varying size and shape opens up the possibility of addressing some of the key microstructural features that govern the hydrotreating activity of Ni_2P and related materials. A collaborative effort between the Brock and Bussell groups is focused on answering questions regarding the effects of metal phosphide particle size, shape and surface functionality on catalytic activity using discrete, solution-prepared Ni_2P particles. In order to probe the effect of surface ligation, Senevirathne et al. conducted Th desulfurization studies of ca. 10 nm unsupported Ni_2P nanoparticles prepared by arrested precipitation of $Ni(COD)_2$ (COD = cyclooctadiene) with TOP in TOPO at 345 °C [20]. The HDS testing of as-prepared Ni_2P nanoparticles indicates a greater activity relative to TPR-prepared unsupported Ni_2P: 250 (nmol Th)$(g\,cat)^{-1}\,s^{-1}$ vs. 150 (nmol Th)$(g\,cat)^{-1}\,s^{-1}$ (Fig. 4a). However, X-ray powder diffraction analysis of the post-catalyst product indicates that the phase has changed from Ni_2P to more P-rich (and less active) Ni_5P_4 and NiP_2 phases (Fig. 4b). That is, under the

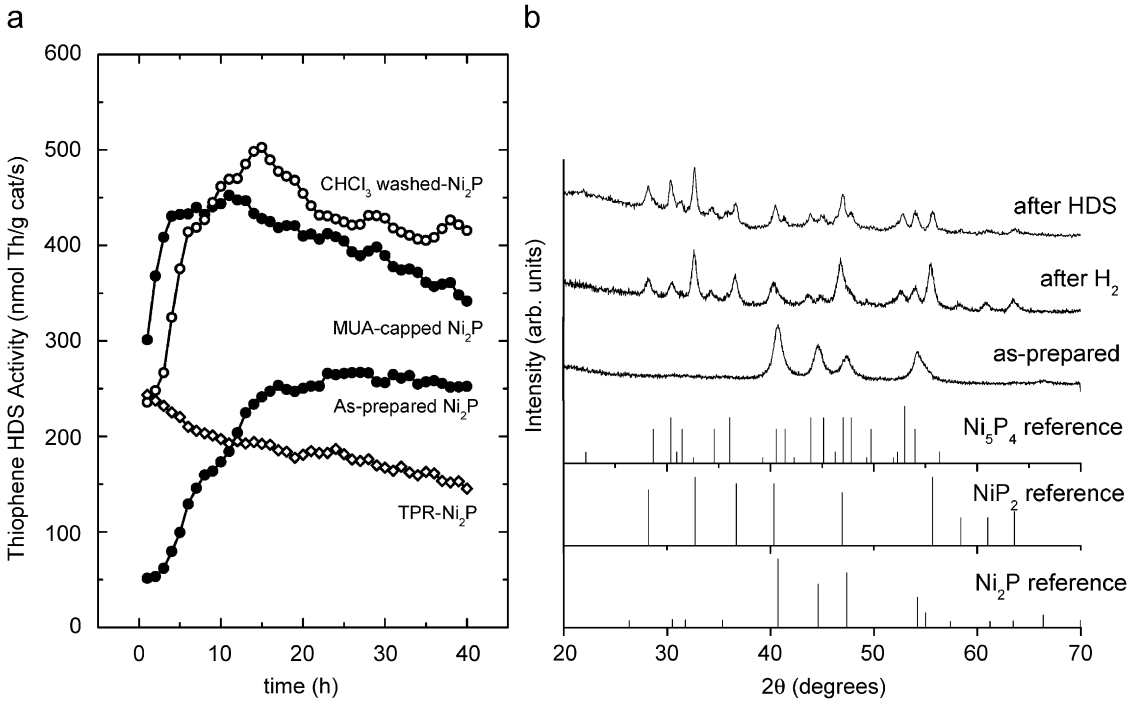

Fig. 4. (a) Graph of HDS activity vs. time of as-prepared, $CHCl_3$-washed, and MUA-capped Ni_2P nanoparticles along with HDS activity of unsupported, TPR-prepared Ni_2P. (b) Powder X-ray diffraction patterns of as-prepared Ni_2P nanoparticles before treatment, after treatment with 5% H_2 at 500 °C, and after 20 h of HDS testing. Reference line diagrams are shown for Ni_5P_4, NiP_2 and Ni_2P. Reproduced with permission from Ref. [20] (Copyright 2007 Wiley-VCH Verlag GmbH & Co. KGaA).

elevated temperatures and reducing conditions employed during catalyst testing (370 °C, 3.2 mol% Th in H_2), the P-containing surface ligands are being reduced, and their phosphorus is being incorporated into the catalyst, which may result in reduced activity. Indeed, if the as-prepared Ni_2P is washed with $CHCl_3$ until the Ni:P ratio is 2:1, the Ni_2P structure is retained throughout testing and improved reactivity is observed, 450 (nmol Th) (g cat)$^{-1}$ s^{-1} (Fig. 4a). Alternatively, the phosphorus-containing ligands can be replaced with thiolates by treatment of as-prepared Ni_2P nanoparticles with 11-mercaptoundecanoic acid (MUA) in the presence of a base. The MUA-capped particles have an intermediate activity between as-prepared and $CHCl_3$-washed samples: 350 (nmol Th)(g cat)$^{-1}$ s^{-1} (Fig. 4a) and the structure is also stable to HDS testing. Despite these promising results, silica supported Ni_2P catalysts prepared by TPR have much higher activities, 2250 (nmol Th)(g cat)$^{-1}$ s^{-1} [49]. This can be attributed in large part to the support, which acts to prevent particle sintering. Indeed, X-ray diffraction analysis of unsupported $CHCL_3$-washed Ni_2P nanoparticles after catalytic testing shows a noticeable sharpening in the peaks due to grain growth [20]. Hence, the next key step is to take the pre-formed particles and cast them onto supports for catalytic testing and acquire activity data for nanoparticles of different size and shape. These studies are the focus of current efforts between the Brock and Bussell groups.

5. Conclusions and prospectus

Recent advances in synthetic methods have led to the preparation of a wide array of transition metal phosphide nanoparticles, and characterization of these materials has provided insight into nanoscale magnetic and catalytic properties. Nevertheless, a number of unanswered questions remain. In a phase diagram with multiple possible phases and stoichiometries, what governs which phase is produced? To what extent are the observed magnetic properties intrinsic to the phases, and to what extent do they represent surface or impurity contributions? What are the key factors that govern HDS activity of transition metal phosphides, and can discrete nanoparticles play a role in elucidating these? Despite all the work of the past 4 years, our synthetic acumen and understanding of the role of size and morphology on the structure–property relationships in these materials remains cursory at best. However, the information gained to date suggests the promise of these materials, which has led to the considerable recent interest, is being fulfilled.

Acknowledgment

Support of the National Science Foundation (DMR-0701161) is acknowledged.

References

[1] H. Fujii, T. Hōkabe, T. Kamigaichi, T. Okamoto, J. Phys. Soc. Jpn. 43 (1977) 41–46.
[2] G. Boda, B. Stenstrom, V. Sagredo, O. Beckman, B. Carlsson, S. Rundqvist, Phys. Scr. 4 (1971) 132–134.
[3] W. Wong-Ng, W.Y. Ching, Y.-N. Xu, J.A. Kaduk, I. Shirotani, L. Swartzendruber, Phys. Rev. B 67 (2003) 144523.
[4] A. Watcharapasorn, R.C. DeMattei, R.S. Feigelson, T. Caillat, A. Borshchevsky, G.J. Snyder, J.P. Fleurial, J. Appl. Phys. 86 (1999) 6213–6217.
[5] S.T. Oyama, J. Catal. 216 (2003) 343–352.
[6] S.L. Brock, S.C. Perera, K.L. Stamm, Chem. Eur. J. 10 (2004) 3364–3371.
[7] M. Green, Curr. Opin. Solid State Mater. Sci. 6 (2002) 355–363.
[8] S. Liu, X. Liu, L. Xu, Y. Qian, X. Ma, J. Cryst. Growth 304 (2007) 430–434.
[9] H. Hou, Q. Yang, C. Tan, G. Ji, B. Gu, Y. Xie, Chem. Lett. 33 (2004) 1272–1273.
[10] X. Wang, K. Han, Y. Gao, F. Wan, K. Jiang, J. Cryst. Growth 307 (2007) 126–130.
[11] H. Hou, Q. Peng, S. Zhang, Q. Guo, Y. Xie, Eur. J. Inorg. Chem. (2005) 2625–2630.
[12] Y. Ni, A. Tao, G. Hu, X. Cao, X. Wei, Z. Yang, Nanotechnology 17 (2006) 5013–5018.
[13] S.C. Perera, P.S. Fodor, G.M. Tsoi, L.E. Wenger, S.L. Brock, Chem. Mater. 15 (2003) 4034–4038.
[14] S.C. Perera, G.M. Tsoi, L.E. Wenger, S.L. Brock, J. Am. Chem. Soc. 125 (2003) 13960–13961.

[15] J. Park, B. Koo, Y. Hwang, C. Bae, K. An, J.-G. Park, Y.M. Park, T. Hyeon, Angew. Chem. Int. Ed. 43 (2004) 2282–2285.
[16] C. Qian, F. Kim, L. Ma, F. Tsui, P. Yang, J. Liu, J. Am. Chem. Soc. 126 (2004) 1195–1198.
[17] J.-H. Chen, M.-F. Tai, K.-M. Chi, J. Mater. Chem. 14 (2004) 296–298.
[18] J. Park, B. Koo, K.Y. Yoon, Y. Hwang, M. Kang, J.-G. Park, T. Hyeon, J. Am. Chem. Soc. 127 (2005) 8433–8440.
[19] K.A. Gregg, S.C. Perera, G. Lawes, S. Shinozaki, S.L. Brock, Chem. Mater. 18 (2006) 879–886.
[20] K. Senevirathne, A.W. Burns, M.E. Bussell, S.L. Stephanie, Adv. Funct. Mater. 17 (2007) 3933–3939.
[21] Z.A. Peng, X. Peng, J. Am. Chem. Soc. 123 (2001) 1389–1395.
[22] A.T. Kelly, I. Rusakova, T. Ould-Ely, C. Hofmann, A. Luettge, K.H. Whitmire, Nano Lett. 7 (2007) 2920–2925.
[23] A.E. Henkes, Y. Vasquez, R.E. Schaak, J. Am. Chem. Soc. 129 (2007) 1896–1897.
[24] R.-K. Chiang, R.-T. Chiang, Inorg. Chem. 46 (2007) 369–371.
[25] A.E. Henkes, R.E. Schaak, Inorg. Chem. 47 (2008) 671–677.
[26] A.E. Henkes, R.E. Schaak, Chem. Mater. 19 (2007) 4234–4242.
[27] V. Jourdain, E.T. Simpson, M. Paillet, T. Kasama, R.E. Dunin-Borkowski, P. Poncharal, A. Zahab, A. Loiseau, J. Robertson, P. Bernier, J. Phys. Chem. B 110 (2006) 9759–9763.
[28] C.G. Hu, Y. Li, J.P. Liu, Y.Y. Zhang, G. Bao, B. Buchine, Z.L. Wang, Chem. Phys. Lett. 428 (2006) 343–347.
[29] J. Gopalakrishnan, S. Pandey, K.K. Rangan, Chem. Mater. 9 (1997) 2113–2116.
[30] C.M. Sweeney, K.L. Stamm, S.L. Brock, J. Alloys Compd. 448 (2008) 122–127.
[31] K.L. Stamm, S.L. Brock, J. Alloys Compd. (2007).
[32] D.L. Leslie-Pelecky, R.D. Rieke, Chem. Mater. 8 (1996) 1770–1783.
[33] S.A. Majetich, J.H. Scott, E.M. Kirkpatrick, K. Chowdary, K. Gallagher, M.E. McHenry, NanoStruct. Mater. 9 (1997) 291–300.
[34] D. Sellmyer, J.M. Zheng, R. Skomski, J. Phys.: Condens. Matter 13 (2001) R433–R460.
[35] G.P. Felcher, F.A. Smith, D. Bellavance, A. Wold, Phys. Rev. B 3 (1971) 3046–3052.
[36] L. Häggström, A. Narayanasamy, J. Magn. Magn. Mater. 30 (1982) 249–256.
[37] S. Chiba, J. Phys. Soc. Jpn. 15 (1960) 581–585.
[38] H. Liu, P. James, A. Broddefalk, Y. Andersson, P. Granberg, O. Eriksson, J. Magn. Magn. Mater. 189 (1998) 69–82.
[39] E.E. Huber Jr., D.H. Ridgley, Phys. Rev. 135 (1964) A1033–A1040.
[40] R.H. Kodama, S.A. Makhlouf, A.E. Berkowitz, Phys. Rev. Lett. 79 (1997) 1393–1396.
[41] J.A. Aitken, G.M. Tsoi, L.E. Wenger, S.L. Brock, Chem. Mater. 19 (2007) 5272–5278.
[42] H. Topsøe, B. Clausen, F.E. Massoth, in: J.R. Anderson, M. Boudart (Eds.), Catalysis: Science and Technology, vol. 11, Springer, Berlin, 1996, pp. 1–310.
[43] L. Song, W. Li, G. Wang, M. Zhang, K. Tao, Catal. Today 125 (2007) 137–142.
[44] S. Yang, C. Liang, R. Prins, J. Catal. 241 (2006) 465–469.
[45] I.I. Abu, K.J. Smith, Appl. Catal A 328 (2007) 58–67.
[46] Y. Shu, S.T. Oyama, Chem. Commun. (2005) 1143–1145.
[47] S. Yang, R. Prins, Chem. Commun. (2005) 4178–4180.
[48] Y. Shu, Y.-K. Lee, S.T. Oyama, J. Catal. 236 (2005) 112–121.
[49] K.A. Layman, M.E. Bussell, J. Phys. Chem. B 108 (2004) 15791–15802.
[50] H. Loboué, C. Guillot-Deudon, A.F. Popa, A. Lafond, B. Rebours, C. Pichon, T. Cseri, G. Berhault, C. Geantet, Catal. Today 130 (2008) 63–68.
[51] A. Montesinos-Castellanos, T.A. Zepeda, B. Pawelec, J.L.G. Fierro, J.A. de Reyes, Chem. Mater. 19 (2007) 5627–5636.
[52] A. Montesinos-Castellanos, E. Lima, J.A. de los Reyes H, V. Lara, J. Phys. Chem. C 111 (2007) 13898–13904.
[53] A. Montesinos-Castellanos, T.A. Zepeda, B. Pawelec, E. Lima, J.L.G. Fierro, A. Olivas, J.A. de los Reyes H, Appl. Catal. A 334 (2008) 330–338.
[54] T.I. Korányi, Z. Vít, J.B. Nagy, Catal. Today 130 (2008) 80–85.
[55] T.I. Korányi, Z. Vít, D.G. Poduval, R. Ryoo, H.S. Kim, E.J.M. Hensen, J. Catal. 253 (2008) 119–131.
[56] S.J. Sawhill, K.A. Layman, D.R. Van Wyk, M.H. Engelhard, C. Wang, M.E. Bussell, J. Catal. 231 (2005) 300–313.
[57] Y. Li, M.A. Malik, P. O'Brien, J. Am. Chem. Soc. 127 (2005) 16020–16021.
[58] R. Fruchart, A. Roger, J.P. Senateur, J. Appl. Phys. 40 (1969) 1250–1257.